RSC
Applied Interfaces

Accepted Manuscript

This article can be cited before page numbers have been issued, to do this please use: T. Zhao, S. Li, Y. Yang, L. Zhao, J. Chen, C. Yu, C. Zhao and G. Xing, *RSC Appl. Interfaces*, 2026, DOI: 10.1039/D6LF00112B.

View Article Online
DOI: 10.1039/D6LF00112B

ARTICLE

$Ti_3C_2T_X$/Graphene Aerogels for High-Efficiency Hydrovoltaic Power Generation: Performance Optimization and Mechanism Elucidation

Tianran Zhao[a†], Sai Li[b†], Yi'na Yang[a], Liyang Zhao[a], Jia Chen[a], Chunna Yu[c], Chang Zhao[c], Guangjian Xing[a*]

Abstract: The global energy shortage crisis underscores the urgent need for sustainable power generation technologies. This study focuses on the hydrovoltaic performance and underlying mechanism of $Ti_3C_2T_X$/graphene aerogels (TGAs). The TGAs were fabricated via hydrothermal treatment followed by freeze-drying, which results in a three-dimensional porous microstructure with a large specific surface area, low density, and abundant surface functional groups. TGAs demonstrated exceptional hydrovoltaic power generation performance, with a maximum output power density of 14.59 mW cm^{-3}, outperforming many reported hydrovoltaic materials. The performance of TGAs was systematically evaluated under varying sunlight intensities, in different electrolyte solutions, and with TGAs containing different $Ti_3C_2T_X$-to-graphene mass ratios. The underlying mechanism was elucidated based on the Stern model of electric double layers, which linked the enhanced performance to increased surface charge density from cation adsorption and the conductive framework of $Ti_3C_2T_X$. Notably, this study introduced a novel interfacial modification mechanism using dye molecules. Performance tests in dye-containing solutions revealed that the output voltage in the Congo red (CR) + $CaCl_2$ mixture was higher than that in pure $CaCl_2$ solution, attributed to synergistic effects between the dye molecules and the electrolyte. This work provides new insights into the design of efficient hydrovoltaic materials.

Keywords: $Ti_3C_2T_X$; graphene; aerogels; hydrovoltaic power generation; adsorption

1. Introduction

The global energy landscape is undergoing unprecedented challenges, with electricity shortages emerging as a critical bottleneck for economic development and social stability. In recent years, soaring energy demand driven by industrial expansion, urbanization, and extreme weather events has exceeded supply capacity in many regions [1, 2]. According to recent estimates, approximately 730 million people worldwide still lack access to electricity, with 600 million of them concentrated in sub-Saharan Africa, while even developed regions face frequent grid disruptions and supply gaps due to increasingly erratic climate patterns and soaring power consumption [3]. Against this backdrop, the quest for sustainable alternatives has intensified. Water covers 71% of the Earth's surface and absorbs 35% of the solar energy reaching the planet, encompassing immense untapped potential in forms such as raindrops, flowing water, evaporation, and atmospheric humidity [4]. Against this backdrop, hydrovoltaic technology has emerged as a transformative solution to address the electricity shortage crisis [5]. This technology generates electricity through direct interactions between functional materials and various forms of water,

View Article Online
DOI: 10.1039/D6LF00112B

eliminating the need for large-scale engineering projects and enabling flexible deployment in diverse environments [6]. However, a critical bottleneck persists in hydrovoltaic energy-harvesting systems: existing hydrovoltaic materials, including carbon black [7], active carbon [8], carbon nanotubes [9], and semiconductor oxides [10], still suffer from inadequate power output that fails to meet practical application requirements. Specifically, their output voltage typically remains below 200 mV, with current confined to the microampere range, resulting in low power density that restricts scalable deployment [11]. Most notably, to date, reported hydrovoltaic material systems only generate electricity in pure water or ion-containing solutions, with no relevant studies conducted on real wastewater—such as dye wastewater. Critically, the underlying hydrovoltaic mechanism remains unclear, which further hinders the optimization of hydrovoltaic performance. Therefore, there is an urgent need to develop functional hydrovoltaic materials capable of achieving efficient energy harvesting while clarifying the intrinsic hydrovoltaic mechanism.

In the fields of hydrovoltaic power generation, emerging nanomaterials such as $Ti_3C_2T_X$ MXene [12, 13] and graphene [14] have garnered significant attention due to their unique advantages. As a representative two-dimensional (2D) transition metal carbide/nitride, $Ti_3C_2T_X$ MXene exhibits exceptional intrinsic properties tailored for hydrovoltaic generation: its metallic-like electrical conductivity facilitates efficient charge transport [15, 16], while abundant surface functional groups (-OH, -O, -F) enable strong interactions with electrolyte ions [17, 18]. Additionally, $Ti_3C_2T_X$ possesses excellent mechanical flexibility and inherent hydrophilicity, ensuring robust structural integrity and intimate water-material interface contact—critical prerequisites for sustained hydrovoltaic performance [19]. Graphene aerogels (GAs) feature a highly interconnected three-dimensional (3D) porous framework, large specific surface area, and robust structural stability, which accelerate water infiltration, promote fast ion diffusion, and offer abundant active sites for interfacial charge separation in hydrovoltaic systems [20]. Accordingly, $Ti_3C_2T_X$/graphene aerogels (TGAs) rationally integrate the exceptional conductivity, high surface charge density, and strong ion affinity of $Ti_3C_2T_X$ with the 3D porous architecture, large surface area, and structural robustness of GAs. Such a hierarchical architecture effectively inhibits the restacking of individual 2D nanosheets and establishes a highly interconnected conductive network with abundant pore channels [21]. For hydrovoltaic application, the porous scaffold accelerates water transport and ion diffusion; while the composite's superior hydrophilicity maintains persistent surface wetting, thereby synergistically enhancing interfacial charge generation and transfer [22]. In this regard, TGAs overcome the performance limitations of single MXene or carbon materials, representing a highly competitive candidate for efficient hydrovoltaic energy harvesting. However, to date the hydrovoltaic power generation performance of TGAs and its underlying mechanism remain insufficiently explored.

Herein, this study aims to explore the potential applications and underlying mechanisms of TGAs in hydrovoltaic energy harvesting. The TGA samples were fabricated via a facile combination of hydrothermal treatment and freeze-drying. The as-prepared TGAs exhibit a microporous structure characterized by a large specific surface area, high porous volume, and low density. Notably, the aerogels deliver exceptional hydrovoltaic power generation performance. The maximum output power density reaches 14.59 mW cm^{-3}. Various factors influencing the hydrovoltaic properties were systematically investigated, and the intrinsic mechanisms were thoroughly explored based on electric double layers (EDLs). Importantly, based on the results of the hydrovoltaic performance of TGAs in dye-containing solutions outperforming that in dye-free solutions, we propose an interfacial modification mechanism via dye molecules to enhance hydrovoltaic efficiency, which has yet been reported. This work provides valuable insights into the synergistic design of efficient hydrovoltaic materials, offering a viable approach to address the energy challenge.

2. Experimental

2.1 Materials. The Ti_3AlC_2 precursor (≥99.9%, 400 mesh) was obtained from Foshan Xin Xi Technology Co., Ltd. A graphene oxide (GO) dispersion (5 mg mL^{-1}) was purchased from Nanjing Jicang Nano Technology Co., Ltd. Lithium fluoride (LiF, 99.0%), ascorbic acid (99.0%), and tetracycline hydrochloride (TCH, 96.0%) were purchased from Aladdin Reagent Co., Ltd. in Shanghai. Congo red (CR) and methylene blue (MB) were obtained from the Beijing Chemical Plant as analytical reagents.

2.2. Fabrication of TGAs. To fabricate TGAs with different $Ti_3C_2T_X$ contents, different volumes (1, 2, and 4 mL) of the as-prepared $Ti_3C_2T_X$ dispersion (25 mg mL^{-1}) were separately mixed with 10 mL of GO dispersion, corresponding to $Ti_3C_2T_X$-to-GO mass ratios of 1:2, 1:1, and 2:1, respectively. After stirring the mixture at room temperature for 10 min, 0.1 g of ascorbic acid was added as a reducing agent. The mixture was stirred for another 10 min before being transferred to a 20 mL Teflon-lined autoclave. This autoclave was sealed and heated at 140°C for 10 h to form $Ti_3C_2T_X$/graphene hydrogels. Subsequent freeze-drying for 72 h yielded TGAs, which were labeled as TGA-1/2, TGA-1/1, and TGA-2/1 (corresponding to the aforementioned $Ti_3C_2T_X$ to GO mass ratios). Attempts to fabricate TGAs with higher $Ti_3C_2T_X$ content than 2:1 resulted in structural collapse, cracking, and failure to form intact monolithic scaffolds. For control experiments, pure graphene aerogels (GAs) were also prepared following the identical procedure but without the addition of $Ti_3C_2T_X$ dispersion.

2.3 Characterization. Field emission scanning electron microscopy (FESEM, SU8020, Hitachi) was utilized to observe the morphology of TGAs. The crystalline phase analysis was performed using an X-ray diffractometer (XRD, Dmax-2600, Rigaku) with a 2θ angle scan range of 5-70°. Fourier transform infrared spectroscopy (FTIR)

---

[a] College of New Materials and Chemical Engineering, Beijing Institute of Petrochemical Technology, Beijing 102617, China. Email: xingguangjian@bipt.edu.cn
[b] China Building Materials Academy, Beijing 100024, China
[c] Zhiyuan School of Liberal Arts, Beijing Institute of Petrochemical Technology, Beijing 102617, China
† These authors contributed equally to this work.

spectra were collected on a Nicolet 6700 FTIR spectrometer (Thermo Fisher Scientific) using the potassium bromide pellet technique, with a scanning range of 4000–400 cm^{-1}. Raman spectroscopy was performed using LabRAM HR800 (Horiba Jobin Yvon) with the wavenumber range from 200 to 3500 cm^{-1}. The surface charge was measured using an electrophoretic light scattering method with a zeta potential analyzer (Zetasizer Nano ZS90, Malvern). Nitrogen adsorption/desorption isotherms were determined using a fully automated specific surface area and porosity analyzer (BET, 3Flex, Micromeritics).

2.4. Electricity generation test. The test configuration diagram for electrical energy generation is shown in Scheme 1. Conductive copper tape electrodes were firmly affixed to the top and bottom surfaces of TGAs. The assembled TGAs were positioned in a test cell holding various aqueous electrolyte solutions, specifically NaCl, LiCl, and $CaCl_2$ solutions. In the testing process, the lower electrode was completely immersed in the electrolyte, while the upper copper electrode was maintained in contact with air. A digital multimeter (VICTOR 8246B) was connected to the two electrodes to measure the electrical output. Simulated sunlight was provided by a xenon lamp (PLSSXE300, Perfectlight, Beijing), with the power density meticulously calibrated using an optical power meter (CEL-NP2000-2A, Ceaulight, Beijing). To minimize experimental errors, triplicate measurements were performed.

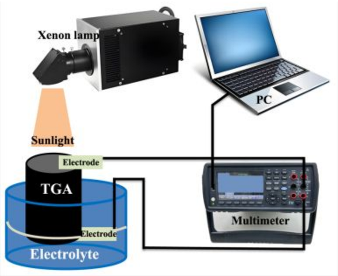

Scheme 1. Schematic illustration of the experimental setup for hydrovoltaic performance testing.

3. Results and discussion

As the similar structural characteristics of all TGA samples, TGA-1/2 is representative in terms of structural properties. Fig. 1a presents the FESEM image of TGA-1/2, revealing a hierarchical porous structure composed of graphene and $Ti_3C_2T_X$ nanosheets. The inset in Fig. 1b displays the macroscopic appearance of TGA-1/2, exhibiting a cylindrical shape with dimensions of approximately 22 mm in diameter and 26 mm in height. The mass of the TGA-1/2 sample was only 0.1530 g, corresponding to a calculated density of 15.5 mg cm^{-3}. This porous structure coupled with low density facilitates rapid mass transfer and provides abundant active sites for ionic interactions. The Energy Dispersive Spectrometer (EDS) analysis in Fig. 1b confirms the presence of Ti, C, O, and F elements in the composite, consistent with the chemical composition of $Ti_3C_2T_X$ and graphene. Furthermore, the elemental mappings (Fig. 1c) demonstrate the homogeneous distribution of Ti and C elements, providing strong evidence for the successful integration of $Ti_3C_2T_X$ nanosheets within the GA matrix.

View Article Online
DOI: 10.1039/D6LF00112B

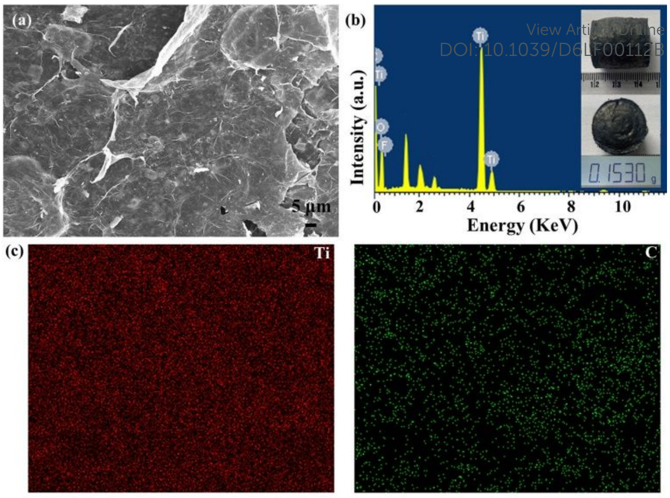

Fig. 1 (a) FESEM image, (b) EDS (inset: digital photographs), and (c) elemental mappings of TGA-1/2.

Fig. 2a displays the XRD patterns of Ti_3AlC_2, $Ti_3C_2T_X$, and TGA-1/2. The Ti_3AlC_2 precursor exhibits distinct diffraction peaks at 9.07°, 18.64°, 33.56°, 36.28°, 38.32°, 41.28°, 48.02°, and 55.98°, and 59.71° corresponding to the (002), (004), (101), (103), (104), (105), (107), (108), and (110) planes of hexagonal Ti_3AlC_2 (JCPDS card No. 52-0875) [23]. After etching, the $Ti_3C_2T_X$ pattern shows the disappearance of most Ti_3AlC_2 peaks, with the (002) peak shifting to a lower angle (~6.22°), confirming the successful preparation of $Ti_3C_2T_X$ with an increased interlayer spacing [24]. TGA-1/2 displays a broad diffraction peak around ~26.0°, corresponding to (002) plane of graphite, indicating the formation of an amorphous structure [25]. Fig. 2b presents the FTIR spectra of TGA-1/2. The broad adsorption band at 3430 cm^{-1} is attributed to the O-H stretching vibration, while the peaks at 1626, 1384, and 1108 cm^{-1} are attributed to C=O stretching, C-H bending, and C-O stretching vibrations, respectively [26]. The presence of abundant functional groups is attributed to the presence of $Ti_3C_2T_X$ nanosheets, as they possess -OH and -COOH groups, which endows the excellent hydrophilicity of TGAs (as shown in inset of Fig. 2b) and thus facilitate the transport of water within the nanopores of TGAs. Fig. 2c presents the Raman spectra of GA and TGA-1/2. In the range of 750–2000 cm^{-1}, both materials exhibit similar Raman peaks, which can be attributed to their analogous carbon-based composition. The characteristic peaks at 1341 cm^{-1} (D band) and 1581 cm^{-1} (G band) are consistent with typical carbon structures [26, 27]. Notably, TGA-1/2 shows a significantly higher I_D/I_G ratio (1.46) compared to pristine GA (1.25), indicating a substantial increase in structural defects upon $Ti_3C_2T_X$ nanosheet incorporation. This enhanced defect density introduces additional disorder in TGAs structure, thereby creating more active sites—a key factor contributing to their enhanced ion adsorption capacity and selectivity.

As shown in Fig. 3a, the N_2 adsorption–desorption isotherm of the TGA-1/2 sample matches a typical Type IV profile with a distinct hysteresis loop, a hallmark feature of mesoporous materials. The specific surface area of TGA-1/2 is calculated to

View Article Online
DOI: 10.1039/D5LF00112B

be ~17.10 m^2 g^{-1}, which is substantially higher than that of pristine GA (12.64 m^2 g^{-1}). This pronounced enhancement is ascribed to the introduction of $Ti_3C_2T_X$ nanosheets, which not only create extra active sites but also inhibit the restacking of graphene nanosheets. The corresponding pore size distribution curve of TGA-1/2, derived from the Barrett–Joyner–Halenda (BJH) model, is illustrated in Fig. 3b. The curve displays a sharp peak centered at 4.1 nm and a broad distribution with a secondary peak at 21.3 nm, extending up to ~50 nm; these two pore populations are assigned to the $Ti_3C_2T_X$ nanorods and the aerogel network, respectively. Such hierarchical pore architecture is highly conducive to water transport for hydrovoltaic power generation.

The hydrovoltaic power generation performance of TGAs was firstly evaluated in different electrolyte solutions under varying sunlight irradiation. Fig. 4 illustrates the output voltage profiles of the TGA-1/2 sample under varying sunlight intensities (1, 2, and 3 sun) in deionized water, 3.5 wt% NaCl, 3.5 wt% LiCl, and 3.5 wt% $CaCl_2$ solutions at room temperature (23.0°C) with a relative humidity (RH) of 30%. As presented in Fig. 4a, under 1 sun, the output voltages of TGA-1/2 in all solutions exhibit a common feature, that is, they rise rapidly from 0 mV to a constant value within a relatively short period of time (approximately 10 s). Deionized water produces a lowest output voltage (35.3 mV). In contrast, the output voltage increases sharply in the three electrolyte solutions: reaching 112.1 mV in NaCl solution, 117.5 mV in $CaCl_2$ solution, and a maximum of 151.8 mV in LiCl solution. Under 2 sun (Fig. 4b), the output voltages further elevate to 84.0, 125.4, 139.4, and 158.7 mV for deionized water, NaCl, $CaCl_2$, and LiCl solutions, respectively. Under 3 sun (Fig. 4c), the voltages continue to rise, achieving 89.2, 151.9, 187.4, and 250.7 mV for the corresponding systems. Fig. 4d summarizes the output voltages within the different solutions under different illumination. It is clear that the voltage trend remains consistent across all sunlight intensities, following the persistent order: LiCl solution > $CaCl_2$ solution > NaCl solution > deionized water. Moreover, under identical electrolyte conditions, the output voltage increases monotonically with increasing solar irradiance, confirming that electrolyte ion type and sunlight intensity exert a prominent influence on the hydrovoltaic performance of TGAs.

According to the Stern model of electric double layers (EDLs), the output voltage of EDLs can be rationalized (Eq. 1) [28]:

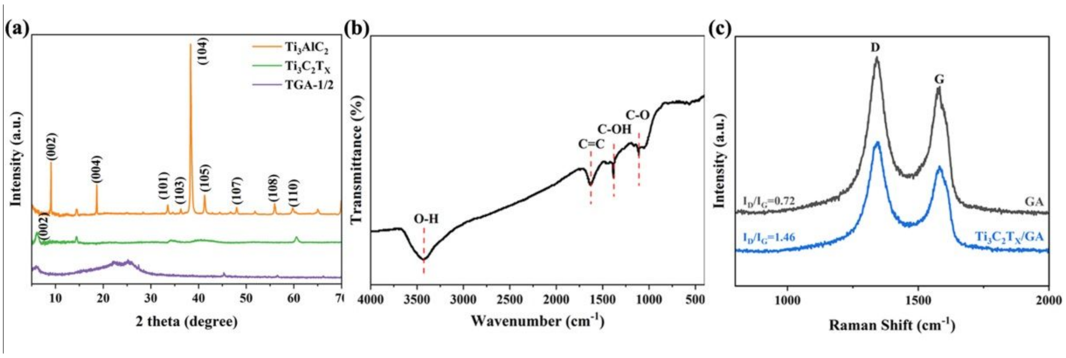

Fig. 2 (a) XRD patterns, (b) FTIR spectra (inset: hydrophilicity), and (c) Raman spectra of TGA-1/2.

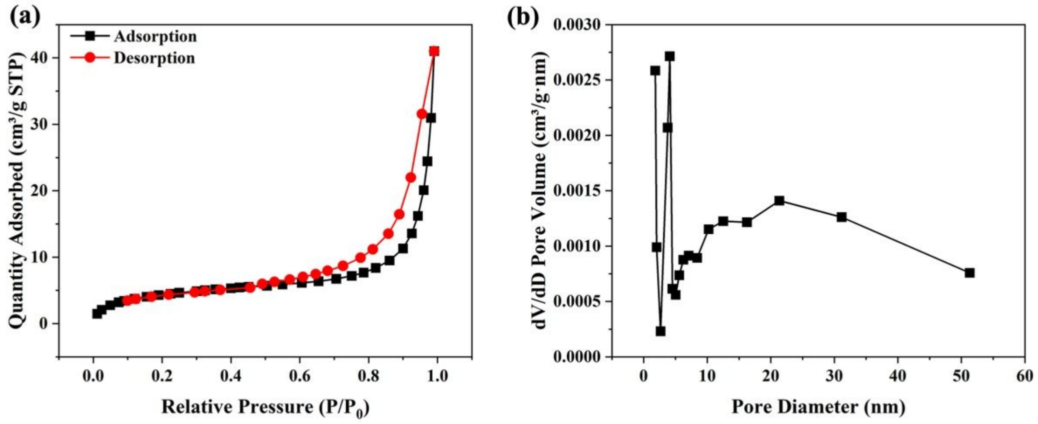

Fig. 3 (a) N_2 adsorption-desorption isotherms and (b) pore diameter distribution of TGA-1/2.

$$V_{EDL} = \frac{\sigma d}{\varepsilon \varepsilon_0}$$

where σ is the surface charge density, d is the thickness of the inner layer, ε is the dielectric constant of the medium, and ε_0 is the dielectric constant of vacuum. According to this model, the EDL voltage is directly proportional to the surface charge density. Therefore, a higher surface charge density gives rise to a larger output voltage. The distinct effects of Li$^+$, Na$^+$, and Ca^{2+} ions on surface charge density are closely associated with their ionic valence and hydration behaviors. Li$^+$ possesses a smaller hydration

View Article Online
DOI: 10.1039/D6LF00112B

radius and higher hydration energy than Na⁺, enabling easier dehydration and tighter adsorption onto the $Ti_3C_2T_X$ MXene surface to form a compact Stern layer, which more effectively elevates the interfacial charge density [12, 28]. Ca^{2+} exhibits moderate hydration radius and hydration energy, and its divalent nature endows it with superior interfacial charge-modulating ability than monovalent Na^+. The synergistic effect of ionic valence and hydration behavior collectively determines the surface charge density and EDL potential, leading to the output voltage sequence of LiCl > $CaCl_2$ > NaCl observed in this work. Consistent with this mechanism, previous simulation results have verified that different cations induce different charge density of $Ti_3C_2T_X$ MXene: Li^+ ions enhances the surface charge density to 0.094 e $Å^{-2}$, whereas Na^+ and Ca^{2+} ions yield values of 0.083 e $Å^{-2}$ and 0.075 e $Å^{-2}$, respectively [12]. The notably higher surface charge density generated by Li^+ adsorption is therefore responsible for the maximum output voltage achieved in the LiCl solution.

Although the EDL model effectively rationalizes the hydrovoltaic output trend, it should be noted that ion diffusion in the porous channels and interfacial ion adsorption occur simultaneously and are strongly coupled during the hydrovoltaic process. The high surface charge density arising from interfacial adsorption provides the driving force for ion migration, while fast ion diffusion within the 3D interconnected porous network of the aerogel maintains continuous charge separation and transport. Due to their synergistic and interdependent nature, it is difficult to fully decouple and quantitatively distinguish the individual contributions of surface adsorption and ion diffusion in the current system. Nevertheless, the combined effect of enhanced interfacial adsorption and accelerated ion diffusion collectively boosts the interfacial potential difference and leads to the excellent hydrovoltaic performance of TGAs.

The positive correlation between solar irradiance and output voltage can be attributed to the synergistic effects of sunlight on charge carrier dynamics and interfacial processes. As sunlight intensity increases, the thermal motion of ions within TGAs and the surrounding electrolyte is accelerated due to the thermal effect caused by the excellent photothermal conversion capabilities of $Ti_3C_2T_X$ [29], which elevates their kinetic energy and promotes faster charge separation and transport at the aerogel-electrolyte interface. Concurrently, higher sunlight intensity facilitates more efficient desorption/adsorption of water molecules and ions on the aerogel's surface, which amplifies the concentration gradient of charge carriers across the interface. These effects synergistically strengthen the built-in electric field induced by the interfacial potential difference, synergistically boosting the output voltage of the hydrovoltaic system.

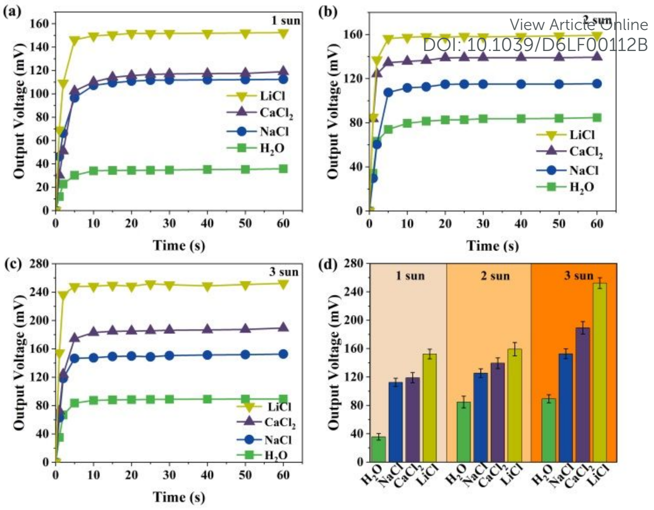

Fig. 4 Output voltages of TGA-1/2 generated in different electrolyte solutions (3.5 wt%) under (a) 1 sun, (b) 2 sun, and (c) 3 sun, and (d) summary of voltages in different solutions under varying sunlight irradiation.

Since the EDLs formed by $Ti_3C_2T_X$ MXene can affect the output voltage, we hypothesize that varying the content of $Ti_3C_2T_X$ MXene in TGAs would also lead to different output voltages. Therefore, we prepared TGAs with different contents of $Ti_3C_2T_X$ MXene and tested their output voltage in $CaCl_2$ solutions. Ca^{2+} was selected primarily because it is a representative divalent cation widely present in natural water, groundwater, and industrial wastewater, making it highly relevant to real-world hydrovoltaic applications. Furthermore, as a divalent ion, Ca^{2+} exhibits unique interfacial coordination interactions with the oxygen-containing functional groups of $Ti_3C_2T_X$, which enables us to systematically investigate the effect of cation valence on the EDL and hydrovoltaic performance. In addition, the hydrovoltaic performance of TGAs in $CaCl_2$ solution remains excellent among the three electrolytes, thus serving as a reliable model system for performance optimization. Fig. 5 depicts the transient output voltage profiles of three TGAs samples (TGA-2/1, TGA-1/1, and TGA-1/2) under 1 sun, 2 sun, and 3 sun in 10.0 wt% $CaCl_2$ solution. Under 1 sun (Fig. 5a), TGA-1/2, TGA-1/1, and TGA-2/1 produce voltage of about 163.0, 189.4, and 268.2 mV, respectively. These samples generate voltages of 228.9, 244.8, and 293.5 mV under 2 sun (Fig. 5b), which further increase to 242.2, 277.5, and 315.8 mV under 3 sun (Fig. 5c). These values are visually displayed in the form of a bar chart in Fig. 5d, indicating a higher proportion of $Ti_3C_2T_X$ in the aerogel corresponding to a larger stable voltage, following the consistent order TGA-2/1 > TGA-1/1 > TGA-1/2 across all tested irradiances. This trend is mirrored in the output current (Fig. 6): TGA-2/1 yields the peak current of about 463.7 μA and stable current of about 124.4 μA under 3 sun. The maximum output power density is calculated to be 14.59 mW cm^{-3}, which surpasses most reported hydrovoltaic power generators (as shown in Table 1) [30-38]. The results shown in Fig. 5 confirm our above speculation. As $Ti_3C_2T_X$ features abundant polar surface functional groups (e.g., -OH, -F), a higher $Ti_3C_2T_X$ proportion (e.g., in TGA-2/1) within TGAs increases the density of these functional groups, thus amplifying the polarization of the interfacial EDLs. This

View Article Online
DOI: 10.1039/D6LF00112B

strengthening of the interfacial EDLs directly elevates the built-in potential difference—the core driving force for rapid transport and accumulation of ions, bringing high voltage and fast response [39]. Additionally, $Ti_3C_2T_X$ exhibits metallic-like electrical conductivity, and increasing its content within the aerogel constructs a more interconnected conductive framework [40]. This network also accelerates the transport of ions and electrons while suppressing their recombination.

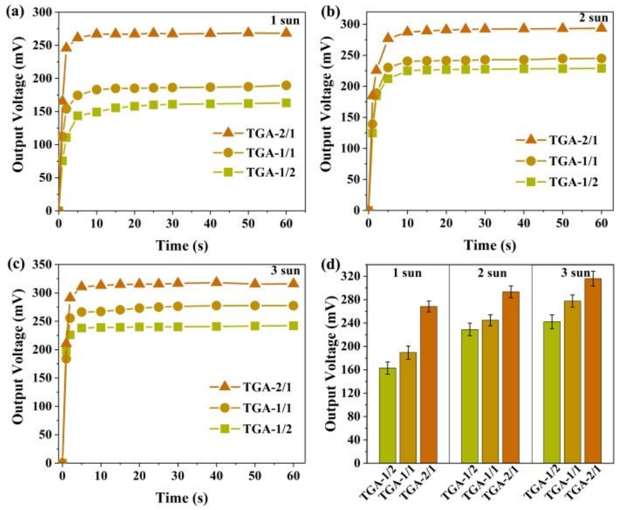

Fig. 5 Output voltage of different TGAs in 10.0 wt% $CaCl_2$ solution under (a) 1 sun, (b) 2 sun, (c) 3 sun, and (d) summary of voltages of different TGAs under varying sunlight irradiation.

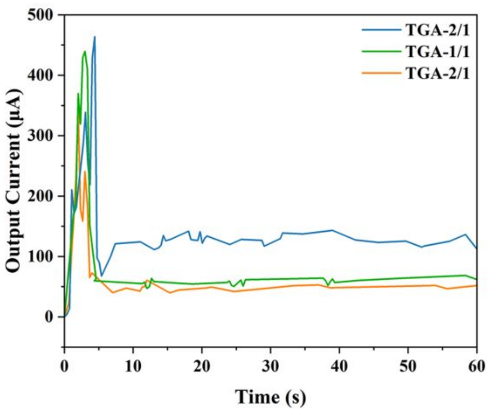

Fig. 6 Output currents of TGAs with 10.0 wt% $CaCl_2$ solution under 3 sun.

Due to the fact that the built-in potential of the electric double layer has both attractive and repulsive effects on ions, the level of ion concentration (i.e., the amount of ions present) will significantly affect the voltage of the EDLs. Therefore, we further investigated the influence of Ca^{2+} ion concentration on the power generation performance of TGAs. The hydrovoltaic performance was evaluated within $CaCl_2$ solution with different concentrations (0, 3.5, 5.0, and 10.0 wt%). Fig. 7 presents the output voltages of TGA-1/2 in these solutions under different sunlight irradiance (1, 2, and 3 sun). Under 1 sun, the sample yields an output voltage of 117.5 mV in 3.5 wt% $CaCl_2$ solution; this voltage increase to 136.8 mV in 5.0 wt% $CaCl_2$ and further rises to 163.0 mV in 10.0 wt% $CaCl_2$. This trend clearly indicates that higher $CaCl_2$ concentration correlate with enhanced voltage output. To validate this concentration-dependent behaviour, voltage measurements were extended to 2 sun and 3 sun irradiances (Figs. 7b and 7c, respectively). Under 2 sun, the output voltages for 3.5, 5.0, and 10.0 wt% $CaCl_2$ solutions are 139.4, 197.5, and 228.9 mV, respectively. At 3 sun, the voltages further increase to 187.4, 208.7, and 242.2 mV for the corresponding concentrations. The summary in Fig. 7d more intuitively shows that elevated Ca^{2+} concentrations promote higher hydrovoltaic output voltages. Additionally, the output voltage of TGA-1/2 increases with increasing solar irradiance across all $CaCl_2$ concentrations—consistent with the trends observed in Fig. 4.

Owing to the abundance of negative functional groups on the surface of $Ti_3C_2T_X$, Ca^{2+} ions are adsorbed onto the surface of $Ti_3C_2T_X$ via strong electrostatic attraction. This adsorption preferentially takes place at the Ti vacancy defect sites of $Ti_3C_2T_X$, leading to the formation of a stable [Ca–O–Ti] coordination structure [40]. The empty orbitals of Ca^{2+} accept the lone pair electrons from oxygen atoms, thereby forming a coordinate covalent bond [42]. This process triggers two key changes: first, the electron cloud of oxygen atoms shifts toward Ca^{2+}, inducing partial deprotonation of the oxygen-containing groups (such as $-OH + H_2O \rightarrow -O^- + H_3O^+$) and the release of additional negative charges [43]; second, the surface Ti atoms of $Ti_3C_2T_X$ undergo d-orbital electron density redistribution due to the enhanced coordination with oxygen, which in turn induces adjacent Ti sites to exhibit stronger electronegativity. Collectively, these effects result in a significant increase in the surface negative charge density of $Ti_3C_2T_X$. According to the Gouy-Chapman-Stern model, the elevated surface charge density directly enhances the built-in potential of the EDLs [28]. As the Ca^{2+} concentration in the $CaCl_2$ solution increases, more Ca^{2+} ions are adsorbed onto the $Ti_3C_2T_X$ surface, further boosting the surface charge density and thus the EDL potential. This enhanced EDL potential facilitates more vigorous ion transport and more efficient charge separation, ultimately leading to a higher hydrovoltaic output voltage. Notably, within the investigated $CaCl_2$ concentration range (0–10 wt%), no obvious performance maximum or turning point is observed, suggesting that the critical concentration for EDL compression and ion mobility restriction has not been reached in this system.

Table 1. Comparison of output performance of TGAs to reported hydrovoltaic materials.

Materials	Output voltage (V)	Output current	Power density	Solution	Ref.
Graphite	0.50	3.2 μA	20.5 μW cm^{-3}	Milli-Q water	30
Surface-modified carbonized silk fabrics	0.288	560 μA cm^{-2}	366 μW cm^{-3}	water	31
PEDOT:PSS-PANI fiber	0.28	8.2 μA	32 μW cm^{-3}	water	32
Cotton fiber rope coated with carbon black	0.66	873 μA	26.4 μW cm^{-3}	1.25 mol L^{-1} $FeCl_3$	33
Janus graphene oxide-cellulose nanofiber membrane	0.55	60 μA	63 μW cm^{-3}	0.6 M NaCl	34
UIO-66/AlOOH film	1.13	427 nA	6.5 μW cm^{-3}	water	35
CNTs/carbon black/PVDF	0.71	700 μA cm^{-2}	2.08 mW cm^{-3}	water	36
Ni-Al LDH	0.7	1.3 μA	16.1 μW cm^{-3}	water	37
Sodium alginate hydrogel	0.19	~1.4 μA	~0.04 μW cm^{-3}	seawater	38
$Ti_3C_2T_X$/graphene aerogel	0.31	463.7 μA	14.59 mW cm^{-3}	10.0 wt% $CaCl_2$	This work

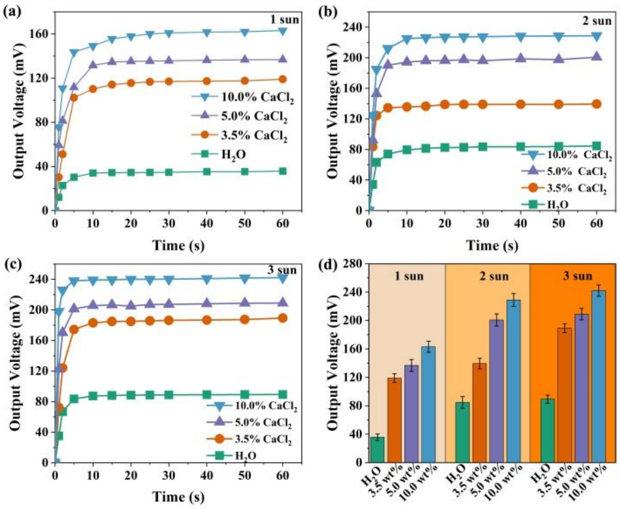

Fig. 7 Output voltages of TGA-1/2 generated in $CaCl_2$ solutions with different concentrations under (a) 1 sun, (b) 2 sun, and (c) 3 sun, and (d) summary of voltage in different $CaCl_2$ solutions under varying sunlight irradiation.

The experimental result that the adsorption of Ca^{2+} ions in TGAs can lead to better power generation performance has inspired us to attempt to modify the TGAs surfaces with other molecules and explore the power generation performance of the modified samples. Due to the extensive use of dyes in modern industry, industrial wastewater contains a considerable amount of residual dyes [44]. Therefore, we attempted to measure the power generation performance of the TGAs samples in wastewater that still contained dyes, in order to investigate the effect of dye modification and evaluate the practical application value of TGAs. Prior to this, adsorption experiments were conducted on various dyes and antibiotic drugs to determine whether the dye molecules can be adsorbed onto the surface of TGAs. The adsorption performance and related mechanism of TGA-1/2 sample for CR and MB dyes are systematically investigated (Fig. 8, Figs. S1-2, Tables S1-2). Notably, kinetic fitting results demonstrate that the adsorption process strictly obeys the pseudo-second-order model with outstanding correlation coefficients (R^2 > 0.99), which unambiguously verifies that chemisorption is the rate-controlling step during dye capture. The TGAs exhibit adsorption capacities of 276.6 mg g^{-1} for CR and 217.2 mg g^{-1} for MB, through electrostatic attraction, hydrogen bonds, and π-π conjugation interactions [45]. Such efficient and chemisorption-dominated dye adsorption serves as a fundamental prerequisite for the subsequent interfacial modification and hydrovoltaic performance enhancement.

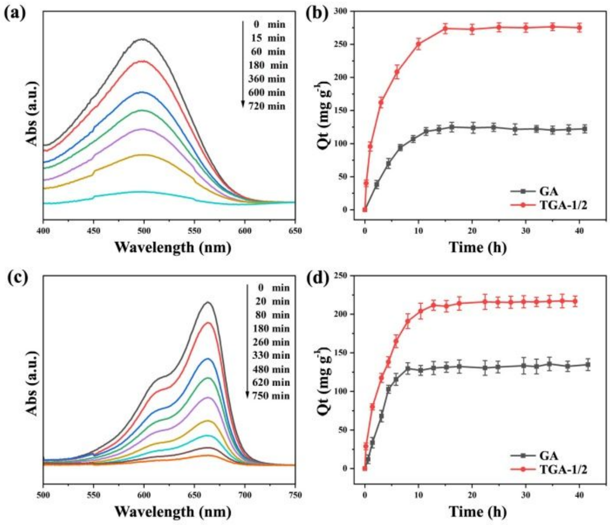

Fig. 8 (a) UV-vis spectra of CR with adsorption time (20 mg, 10 mg L^{-1}, RT), (b) adsorption capacity of TGA-1/2 for CR, (c) UV-vis spectra of MB with adsorption time (20 mg, 10 mg L^{-1}, RT), and (d) adsorption capacity of TGA-1/2 for MB.

The hydrovoltaic voltages generated within dye solutions are illustrated in Fig. 9a, exhibiting the time-resolved output voltages of TGA-1/2 operating in MB, CR, MB + $CaCl_2$, and CR+ $CaCl_2$ aqueous solutions (under 1 sun irradiation). Unlike the voltage profiles in dye-free systems, the curves in these dye solutions show a sustained upward trend. After 60 s of continuous operation, the output voltages reach 164.4 mV in MB + $CaCl_2$ solution, 262.2 mV in CR + $CaCl_2$ solution, 117.0 mV in CR solution, and 84.8 mV in MB solution, respectively. This behaviour is attributed to the time-dependent continuous adsorption of dye species onto the TGA-1/2 interface, which gradually modifies the sample surface and modulates the interfacial charge distribution. The output voltages produced in these mixture solutions and pure dye or $CaCl_2$ solution are illustrated in Fig. 9b. Evidently, all output voltages obtained in dye-containing solutions substantially surpass the reference value in deionized water (35.3 mV, as presented in Fig. 4a). Furthermore, the output voltages within dye and $CaCl_2$ mixture solutions are larger than those within pure $CaCl_2$ solution. And in the CR + $CaCl_2$ solutions, the output voltage is the highest.

The hydrovoltaic mechanism of TGAs within the CR + $CaCl_2$ mixture solutions is shown in Fig. 9c. Although CR is an anionic dye, TGAs can still adsorb it via hydrogen bond and π-π bond (as confirmed by the adsorption data shown in Fig. 8). After the adsorption CR^- ions, their negative charges further increase the surface charge density of EDLs (as confirmed by Fig. S3 which shows that the zeta potential of TGA-1/2 became more negative after adsorption of CR, about -22.87 mV, compared to -22.33 mV before CR adsorption), thus boosting the output voltage. Additionally, the dissociated Na^+ ions from CR also provide extra cationic carriers to facilitate ion migration and further elevate the output voltage. Furthermore, the adsorbed CR molecules with conjugated aromatic structures can form an ordered interfacial molecular layer, which introduces an additional surface potential gradient and optimizes the arrangement of interfacial water molecules. This oriented molecular arrangement effectively promotes charge separation and reduces the energy barrier for interfacial charge transport.

For the MB + $CaCl_2$ solutions, the MB^+ ions can neutralize a portion of the negative surface charge. However, MB molecules possess a planar conjugated structure and high dipole moment. Upon adsorption, MB molecules adopt an ordered arrangement, forming a dense molecular dipole layer, which forces adjacent water molecules to align along the field direction of the dipoles [46, 47]. This alignment generates an additional interfacial potential gradient, which significantly contributes to the total voltage. The effect outweighs charge neutralization from MB cations, finally boosting voltage output.

Collectively, the voltage enhancement in dye-containing electrolyte systems arises from the synergistic coupling of multiple factors: (1) increased surface charge density induced by adsorbed dye species; (2) formation of oriented molecular dipole layers to introduce extra interfacial potential; (3) optimized interfacial water structure and EDL configuration to accelerate charge separation; and (4) supplementary ionic carriers provided by dye dissociation. These interfacial effects work together to amplify the hydrovoltaic output. However, it should be noted that a strict quantitative correlation between dye adsorption capacity and the increment of output voltage cannot be fully established in the present system. This is because the hydrovoltaic enhancement originates from the synergistic coupling of dye adsorption, interfacial charge redistribution, interfacial dipole layer formation, and coexisting ion effects. These multiple factors act simultaneously and are difficult to decouple individually for quantitative analysis. Nevertheless, the consistent trend between dye adsorption and voltage improvement clearly verifies that interfacial dye adsorption plays a key role in boosting the hydrovoltaic performance.

View Article Online
DOI: 10.1039/D6LF00112B

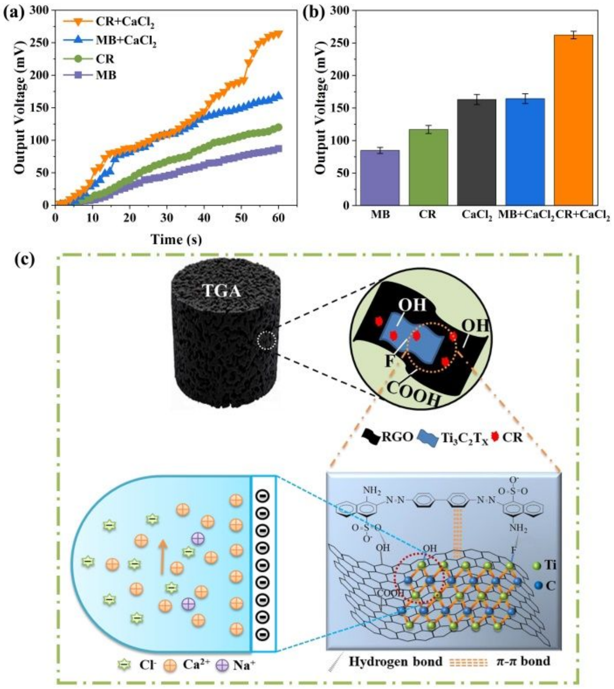

Fig. 9 Output voltages (a) and currents (b) of TGA-1/2 in dye solutions (10 mg L^{-1}) under 1 sun, and (c) scheme of hydrovoltaic power generation of TGA after adsorption of CR dye.

Finally, the long-term operational reliability of the TGAs-based hydrovoltaic generator was evaluated in 10.0 wt% $CaCl_2$ aqueous solution under 1 sun illumination. As depicted in Fig. 10a, the output voltage and stable operating current remain constant over five consecutive cycles (around 160.0 mV and 43.0 μA, respectively), with negligible fluctuations and no obvious performance degradation. To further verify the long-term durability, the TGA sample was stored in ambient environment for one month and then re-tested under identical conditions. As shown in Fig. 10b, the generator still exhibits stable voltage output around 160.0 mV and steady operating current near 40.0 μA during five repeated cycles, which are highly consistent with the fresh sample. These results unambiguously demonstrate the outstanding cyclic stability and long-term durability of the TGAs, which are highly favourable for applications in sustainable hydrovoltaic energy harvesting.

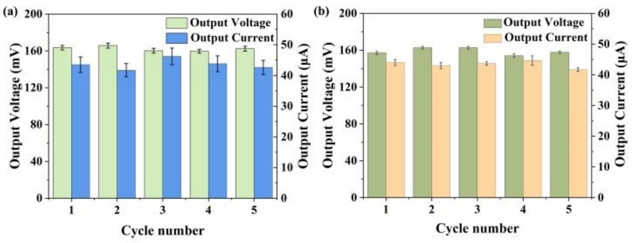

Fig. 10 (a) Cyclic performance of TGA-1/2 in 10.0 wt% $CaCl_2$ solution under 1 sun, and (b) cyclic performance of TGA-1/2 after stored for one month in 10.0 wt% $CaCl_2$ solution under 1 sun.

4. Conclusion

In conclusion, this work successfully developed TGAs as promising materials for hydrovoltaic power generation. Systematic evaluations revealed that the hydrovoltaic performance of TGAs was significantly influenced by multiple factors: electrolyte type, $Ti_3C_2T_X$ content, ion concentration, and sunlight intensity. Notably, the maximum output power density of TGAs reached 14.59 mW cm^{-3} in 10.0 wt% $CaCl_2$ solution, outperforming most reported hydrovoltaic materials. The mechanism of enhanced power generation was rationalized through the EDL model, where $Ti_3C_2T_X$'s abundant surface functional groups and cation adsorption lead to increased surface negative charge density and higher EDL potential and, consequently, greater output voltage. Furthermore, the findings revealed that dye molecules adsorbed onto the TGA surface can further enhance hydrovoltaic efficiency through interfacial modification, contributing an additional potential gradient. This synergistic effect between dyes and ions provides a promising strategy for improving energy harvesting from real wastewater. Finally, TGAs exhibited excellent cyclic stability, ensuring long-term stable operation in practical applications. This work provides valuable insights into the synergistic design of efficient hydrovoltaic materials and offers a viable strategy for simultaneous energy harvesting and pollutant adsorption, opening new avenues for sustainable energy generation in real-world water environments.

Author contributions

T.Z. and S.L. contributed equally. The manuscript was written through the contributions of all authors. All authors have given approval of the final version of the manuscript.

Conflicts of interest

There are no conflicts to declare.

Data availability

The raw/processed data required to reproduce these findings cannot be shared at this time due to technical or time limitations.

Acknowledgements

The authors are grateful for the financial support from the Beijing Natural Science Foundation (1192007) and the Undergraduates Research Training Program of Beijing Institute of Petrochemical Technology (2025J00287).

References

1 E. Nejla, K. Saidani and M. Besbes, *Int. J. Sustain. Energy*, 2025, **44**, 2569922.
2 T. Ramachandran and R.K. Raji, *Sustain. Energy Fuels*, 2026, **10**, 2137–2168.
3 J. Blay, K.C. Seto and T.H.K. Chen, *Remote Sens. Appl.*, 2025, **38**, 101619.
4 I.W. Ock, J. Yin, S. Wang, X. Zhao, J.M. Baik and J. Chen, *Adv. Energy Mater.*, 2025, **15**, 2400563.
5 G. Zan, S. Li, K. Zhao, H. Kim, E. Shin, K. Lee, J. Jang, G. Kim, Y. Kim, W. Jiang, T. Kim, W. Kim and C. Park, *Energ. Environ. Sci.*, 2025, **18**, 53.
6 C. Gu, Y. Luo, H. Ji, S. Wang, B.Y. Huang, X. Zhu and L. Wang, *Adv. Sustain. Syst.*, 2025, 9, 2400805.
7 S. Jiao, Y. Zhang, X. Hou, X. Liu and X. Zhou, *Renew. Energ.*, 2026, **256**, 123945.
8 S. Lal and S.K. *Batabyal, J. Power Sources*, 2023, **568**, 232951.
9 R. Kumar, T. Tabrizizadeh, S. Chaurasia, G. Liu and K. Stamplecoskie, *Sustain. Energ. Fuels*, 2022, **6**, 1141.
10 J. Li, R. Wang, C. Wang, Y. Xu, W. Cheng, J. Wang, G. Zhao, X. Du, H. Yang, G. Ma, Y. Xu, Y. Ye, L. Li, Y. Sun, J. Zhao, R. Tang and G. Zou, *Adv. Funct. Mater.*, 2025, **35**, 2421130.
11 J.H. Park, S.H. Park, J. Lee and S.J. Lee, *ACS Sustainable Chem. Eng.*, 2021, **9**, 5027.
12 J. Bae, M.S. Kim, T. Oh, B.L. Suh, T.G. Yun, S. Lee, K. Hur, Y. Gogotsi, C.M. Koo and I.D. Kim, *Energy Environ. Sci.*, 2022, **15**, 123.
13 G. Kim, K. Zhao, S. Li, G. Zan, E. Shin, M. Kwon and C. Park, *Commun. Mater.*, 2025, **6**, 158.
14 Y. Gao, T. He, X. Cai, W. Xiao, J. Tang, Y. Zhao, H. Fu, K. Fan, M. Qin and J. Cai, *New Carbon Mater.*, 2025, **40**, 1016–1037.
15 Y.A. Kumar, R.M.N. Kalla, R. Khan, A.G. Al-Sehemi, A. Ghosh, T. Ramachandran and J. Lee, *J. Power Sources*, 2026, **665**, 239027.
16 T. Ramachandran, L. Zheng, H. Butt and M. Rezeq, *Mater. Today Adv.*, 2026, **29**, 100675.
17 M. Hu, T. Hu, Z. Li, Y. Yang, R. Cheng, J. Yang, C. Cui and X. Wang, *ACS Nano*, 2018, **12**, 3578–3586.
18 T. Ramachandran, R.M.N. Kalla, R. Khan, A.G. Al-Sehemi, Y.A. Kumar, A.K. Yadav and J. Lee, *J. Power Sources*, 2026, **664**, 238945.
19 P. Liu, H. Liu, T. Zhang, L. Chen, W. Guo, T. Gu, F. Yu, Y. Liu and G. Wang, *Chem. Eng. J.*, 2023, **477**, 146913.
20 T. Ramachandran, N. Roy, H.H. Hegazy, I.S. Yahia, Y.A. Kumar, M. Moniruzzaman and S.W. Joo, *J. Alloy. Compd.*, 2025, **1010**, 177248.
21 S. He, P. Zhou, Y. Wang, P. Ji, Y. Wang, Q. Liu, K. Wu, Z. Liu and N. Gu, *J. Mater. Sci.*, 2025, **60**, 15127–15139.
22 B. Zhang, W. Xu, L. Peng, Y. Li, W. Zhang and Z. Wang, *Nat. Rev. Electr. Eng.*, 2024, **1**, 218–233.
23 R.R. Jaiswar, H.S. Nishad, D. Singh, S.P. Patole and P.S. Walke, *J. Mate. Chem. A*, 2026, **14**, 6663–6677.
24 Y. Zhang, C. Tang, S. Lu, Y. Zeng, Q. Hua and Y. Zhang, *Carbon Neutralization*, 2025, **4**, e70006.
25 X. Wu, J. Zhou, W. Xing, G. Wang, H. Cui, S. Zhuo, Q. Xue, Z. Yan and S.Z. Qiao, *J. Mater. Chem.*, 2012, **22**, 23186.
26 M. Guo, L. Cai, D. Han, W. Hao, J. Wu, G. Fang and S. Wang, *ACS Sens.*, 2025, 10, 8683–8693.
27 T. Ramachandran, N.P. Reddy, A.M. Fouda, H.H. Hegazy, A. Maity, P. Ramakrishna, S. S. Rao and Y.A. Kumar, *J. Power Sources*, 2026, **677**, 239925.
28 T.G. Yun, J. Bae, A. Rothschild and I.D. Kim, *ACS Nano*, 2019, **13**, 12703–12709.
29 Z. Li, F. Liu, X. Jing, W. Zhou, S. Pei, T. Abdiryim, F. Xu, J. You, Y. Tan and X. Liu, *Chem. Eng. J.*, 2025, **519**, 165019.
30 R. Kumar, G. Kay, G. Beaton and K. Stamplecoskie, *ACS Appl. Mater. Interfaces*, 2023, **15**, 7511–7517.
31 X. Guo, Y. Zhang, S. Liao, Y. Hao, P. Lv and Q. Wei, *Chem. Eng. J.*, 2025, **522**, 167621.
32 Y. Fang, Z. Wang, P. Zhu, Y. Wu, W. Wu, S. Wang, W. Zeng and L. Ruan, *Sens. Actuators B Chem.*, 2026, **446**, 138651.
33 S. Jiao, Y. Zhang, Y. Li, B. Maryam, S. Xu, W. Liu, M. Liu, J. Li and X. Liu, *Carbon*, 2024, **218**, 118687.
34 J. Eun and S. Jeon, *ACS Appl. Mater. Interfaces*, 2023, **15**, 50126–50133.
35 Q. Ma, Q. He, P. Yin, H. Cheng, X. Cui, Q. Yun and H. Zhang, *Adv. Mater.*, 2020, **32**, 2003720.
36 Y. Liu, Z. Li, L. Wang, X. Yang, Y. Yang, X. Li, Y. Jiang, Y. Gao, W. Lü, *Adv. Funct. Mater.*, 2024, **34**, 2312666.
37 J. Sun, P. Li, J. Qu, X. Lu, Y. Xie, F. Gao, Y. Li, M. Gang, Q. Feng, H. Liang, X. Xia, C. Li, S. Xu, J. Bian, *Nano Energy*, 2019, **57**, 269–278.
38 J. Pei, G. Chen, Z. Li, Z. Zhou, A. Chen, S. Xie, X. Jiang, *Ind. Eng. Chem. Res.*, 2023, **62**, 21666–21672.
39 Y. Lee, M. Lee, J. Lee, H.W. Jang, J.S. Jang, *Exploration*, 2025, **5**, 70007.
40 A. Lipatov, S. Bagheri, A. Sinitskii, *ACS Mater. Lett.*, 2024, **6**, 298–307.
41 J. Sun, Q. Mu, T. Wang, J. Qi, C. Hu, *J. Colloid Interf. Sci.*, 2021, **590**, 539–547.
42 G. Ren, Y. Ha, Y.S. Liu, X. Feng, N. Zhang, P. Yu, L. Zhang, W. Yang, J. Feng, J. Guo, X. Liu, *J. Phys. Chem. B*, 2020, **124**, 3408–3417.
43 H. Song and D. Jiang, *Nanoscale*, 2023, **15**, 16010–16015.
44 T. Islam, M.R. Repon, T. Islam, Z. Sarwar, M.M. Rahman, *Environ. Sci. Pollut. Res.*, 2023, **30**, 9207–9242.
45 P. Najibikhah, H. Shayesteh, A. Rahbar-Kelishami, *J. Mol. Liq.*, 2025, **429**, 127627.
46 Y. Kaneko, N. Iyi, J. Bujdák, R. Sasai, T. Fujita, *J. Mater. Res.*, 2003, **18**, 2639–2643.
47 H. Kumar, S. Bera, S. Dasgupta, A.K. Sood, C. Dasgupta, P.K. Maiti, *Phys. Rev. B*, 2023, **107**, 165402.

View Article Online
DOI: 10.1039/D6LF00112B

Data Availability Statement

All data generated or analyzed during this study are included in this published article and its supplementary information files.